Available online at www.sciencedirect.com
SCIENCE DIRECT
Journal of Catalysis 235 (2005) 272–278
JOURNAL OF CATALYSIS
www.elsevier.com/locate/jcat

Synthesis, characterization and photocatalytic reactivities of Mo-MCM-41 mesoporous molecular sieves: Effect of the Mo content on the local structures of Mo-oxides

Shinya Higashimoto [a], Yun Hu [a], Rie Tsumura [a], Kiyoshi Iino [a], Masaya Matsuoka [a], Hiromi Yamashita [a], Yong Gun Shul [b], Michel Che [c], Masakazu Anpo [a,*]

[a] *Department of Applied Chemistry, Graduate School of Engineering, Osaka Prefecture University, 1-1 Gakuen-cho, Sakai, Osaka 599-8531, Japan*
[b] *Department of Chemical Engineering, Yonsei University, Sodaemun-ku, Shinchon-dong 134, Seoul 120-749, South Korea*
[c] *Laboratoire de Réactivité de Surface, Université P. et M. Curie, UMR7609, CNRS, 4 Place Jussieu, 75252 Paris cedex 05, France*

Received 20 May 2005; revised 6 August 2005; accepted 11 August 2005

Abstract

A series of Mo-MCM-41 mesoporous molecular sieves of varying Mo content were synthesized and the local structures of their active sites characterized by means of XRD, UV–vis, photoluminescence, and XAFS measurements. Mo-MCM-41 was found to possess three different types of Mo-oxide species, the concentrations of which were dependent on the Mo content: a highly dispersed tetra-coordinated monomeric molybdate, a tetra-coordinated dimeric and/or oligomeric molybdate, and a hexa-coordinated polymeric molybdate. Moreover, the tetra-coordinated molybdate species was observed to play a major role in the photocatalytic reduction of NO in the presence of CO to form N_2 and CO_2.

Keywords: Photocatalysis; Mo-MCM-41; Local structure of Mo-oxides; NO reduction; CO

1. Introduction

In the study of catalysis and photocatalysis, detailed characterizations of the active sites at the atomic and structural level are important in understanding the mechanisms that will lead to high reactivity and efficiency [1–9]. Molybdenum catalysts incorporated on various supports such as zeolites (e.g., Mo/HZSM-5 and Mo-oxide/ZrO_2) have been found to be effective in the selective oxidation of CH_4 or C_2H_6 as well as for hydrodesulfurization reactions and the conversion of methane into aromatic compounds such as benzene [10–12]. The structure and reactivity of the supported molybdenum oxide catalysts, as well as the chemical state of the active sites, have been investigated using such spectroscopic techniques as electron paramagnetic resonance (EPR) [13–19], X-ray absorption fine structure (XAFS) [1], UV resonance Raman [20], and photoluminescence (PL) analyses [8,9]. Iglesia et al. reported that solid-state reactions between MoO_3 and H-ZSM-5 at 773–973 K could yield isolated and/or dimeric tetrahedrally coordinated Mo-oxides within the zeolite cavities. In particular, the dimeric tetrahedrally coordinated Mo-oxide species was found to play a significant role in the aromatization of methane [10].

The photochemical properties of molybdates supported on PVG or SiO_2 for the selective oxidation of hydrocarbons and CO oxidation with O_2 have also been investigated [21–33]. In previous work we observed that supported Mo-oxides exhibit a photo-induced metathesis reaction of C_3H_6 to produce C_2H_4 and 2-C_4H_8. In fact, PL spectroscopic analysis showed that the charge transfer-excited triplet state of the highly dispersed tetra-coordinated molybdate played a significant role in the reaction [26,27]. Recently, we developed photocatalysts incorporating transition metal oxides (Ti, Cr, V, Mo) and ions (Cu, Ag) confined within microporous and/or mesoporous zeolites [8,9]. The capacity for incorporation of the large Mo^{6+} ions within the microporous zeolites is limited because of the rigid inorganic framework structure of such materials as ZSM-5,

* Corresponding author.
E-mail addresses: anpo@ok.chem.osakafu-u.ac.jp, anpo@chem.osakafu-u.ac.jp (M. Anpo).

0021-9517/$ – see front matter
doi:10.1016/j.jcat.2005.08.009

whereas hexagonal mesoporous silica molecular sieves (MCM-41), with their high specific surface area, offer greater flexibility in structure than the microporous zeolites and thus allow relatively easy incorporation of Mo ions into their framework. Mesoporous molecular sieves containing a large number of active sites thus can be expected to exhibit high photocatalytic reactivity for various reactions [34–42]. Therefore, investigations into the properties of Mo-oxides with varying Mo content on Mo-MCM-41 are important to understanding the correlation between the local structure of Mo-oxides and the photocatalytic activity.

In this paper we report on (1) the synthesis of Mo-MCM-41 mesoporous molecular sieves with different Mo content; (2) a characterization of Mo-MCM-41 with different local structures for the Mo-oxides by X-ray diffraction (XRD), UV–vis, XAFS, and PL techniques; and (3) the photocatalytic reactivity for NO reduction with CO to form N_2 and CO_2.

2. Experimental

2.1. Preparation of the catalysts

Mo-MCM-41 mesoporous molecular sieves with Si/Mo ratios of 320, 160, 80, and 40 were synthesized using tetraethylorthosilicate and ammonium heptamolybdate [$(NH_4)_6Mo_7O_{24}\cdot 4H_2O$] as the starting materials and cetyltrimethylammonium bromide (CTMABr) as the structure-directing agent [43,44]. The molar composition of the reaction mixture was 1.0 SiO_2:x MoO_3:0.20 $[C_{16}H_{33}N(CH_3)_3]$Br:160 H_2O (x = 0.0031, 0.0063, 0.013, and 0.025 for Si/Mo ratios of 320, 160, 80, and 40, respectively). The pH was adjusted to 0.5 with the HCl solution, and the reaction mixtures were stirred for 5 days at room temperature. After the products were recovered by filtration, washed with distilled water several times, and dried at 373 K for 12 h, the samples were calcinated under a dry flow of air at 773 K for 8 h to remove any organic compounds. Before spectroscopic measurements and photocatalytic reactions, the catalysts were degassed at 773 K for 2 h and calcined in O_2 (>20 Torr) at 773 K for 2 h, then degassed at 473 K for 2 h.

The imp-Mo/MCM-41 catalyst (1.0 wt% as Mo) was prepared by impregnating an aqueous solution of ammonium heptamolybdate into MCM-41. It was dried at 373 K for 12 h, followed by calcination under a dry flow of air at 773 K for 5 h.

2.2. Catalyst characterizations

The powder XRD patterns of the samples were obtained with a Shimadzu XD-D1 using Cu-K_α radiation ($\lambda = 1.5417$ Å). The hexagonal unit cell parameter (a_0) was calculated from $2d/\sqrt{3}$ and a diffraction peak of 100, obtained from 2θ of the first peak in the XRD patterns by the Braggs equation ($2d\sin\theta = \lambda$). The value of a_0 was equal to the internal pore diameter plus one pore wall thickness. The pore sizes of the MCM-41 samples were calculated by subtracting the size of the wall thickness of about 10 Å, as reported by Horvath–Kawazoe [44], from the value of a_0.

The amount of Mo on Mo-MCM-41 was determined with a Shimadzu atomic absorption flame emission spectrophotometer (model AA-6400F). The calcined Mo-MCM-41 mesoporous molecular sieves with Si/Mo ratios of 320, 160, 80, and 40 corresponded to Mo amounts of 0.5, 1.0, 2.0, and 4.0 wt%, respectively. UV–vis spectroscopic measurements were carried out on a Shimadzu UV–vis recording spectrophotometer (model UV-2200A). The PL and lifetimes were measured at 77 K with a Shimadzu RF-501 spectrofluorophotometer and an apparatus for lifetime measurements, respectively.

The XAFS (XANES and EXAFS) spectra were obtained at the BL-10B facility of the High-Energy Acceleration Research Organization (KEK) in Tsukuba, Japan. The storage ring energy was set at 2.5 GeV, and the positron current was 250–350 mA. The XAFS spectra of the dehydrated samples were recorded at Mo K-edge absorption in the transmittance mode at 295 K. The EXAFS data were examined by an EXAFS analysis program, Rigaku EXAFS (REX). Fourier transform was performed on k^3-weighted EXAFS oscillations in the region of 3–10 $Å^{-1}$ to obtain the radial structure functions.

2.3. Photocatalytic reactions

The photocatalytic reduction of NO with CO into N_2 and CO_2 was performed under a closed system. Typically, 80 mg of the sample was loaded in a quartz cell with a flat bottom (35 mL) connected to a vacuum system (10^{-3} Torr range). After pretreatment, NO and the reducing gases (180 μmol g_{cat}^{-1}) were introduced into the quartz cell. UV irradiation was carried out using a high-pressure mercury lamp (75 W) through a UV cut filter ($\lambda > 270$ nm) at 295 K, with a water bath used to keep the flat bottom at a constant temperature. The products were then analyzed by an on-line gas chromatograph equipped with a thermal conductivity detector for analysis of N_2, N_2O, CO, CO_2, and other elements.

3. Results

3.1. Characterizations of Mo-MCM-41

3.1.1. XRD studies

As the Mo content increased, the color of the as-synthesized samples changed from white to pale yellow, and that of the calcined samples changed from white to pale green. As shown in Fig. 1, the XRD patterns of the calcined Mo-MCM-41 (0.5, 1.0, 2.0, and 4.0 wt%) and silicious MCM-41 exhibited well-defined 100 diffractions accompanied by broader, unresolved higher-order reflections, indicating that they have hexagonal MCM-41 mesostructures. The 100 diffraction attributed to Mo-MCM-41 showed a shift toward lower degrees than that for silicious MCM-41. Table 1 summarizes the d_{100}, hexagonal unit cell parameters (a_0), and specific BET surface area for all of the samples. The pore size of Mo-MCM-41 was observed to increase from 32.3 to 37.8 Å on incorporation of Mo-oxides into the meso-frameworks. An increase in the unit cell size parameter was also noted on the incorporation of Cr ions into the MCM-41 and HMS frameworks, in good agreement with the

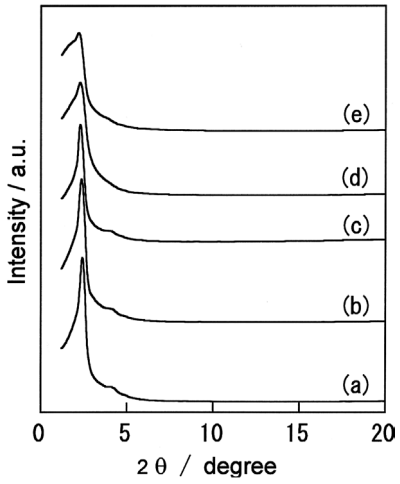

Fig. 1. XRD patterns of the silicious MCM-41 (a) and Mo-MCM-41 with different Mo contents of (a) 0.5, (b) 1.0, (c) 2.0, and (d) 4.0 wt%.

Table 1
Hexagonal unit cell parameters and BET specific surface areas of Mo-MCM-41 with different Mo contents and imp-Mo/MCM41(1.0)

Samples (wt% as Mo)	d_{100} (Å)	a_0 (Å)	S_{BET} ($m^2\ g^{-1}$)
MCM-41	36.6	42.3	1086.5
Mo-MCM-41 (0.5)	36.9	42.6	1007.6
Mo-MCM-41 (1.0)	38.1	44.0	1002.4
Mo-MCM-41 (2.0)	39.2	45.3	987.7
Mo-MCM-41 (4.0)	41.4	47.8	945.4
imp-Mo/MCM-41 (1.0)	37.6	43.4	672.0

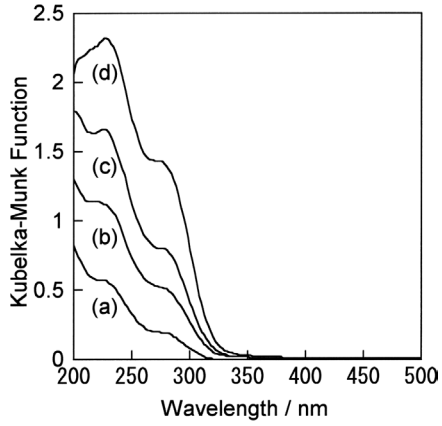

Fig. 2. Diffuse reflectance UV–vis spectra of Mo-MCM-41 with different Mo contents of (a) 0.5, (b) 1.0, (c) 2.0, and (d) 4.0 wt%.

data from previous analyses [43,45]. A specific BET surface area of about 1000 $m^2\ g^{-1}$ was retained on Mo-MCM-41 in the range of 0.5–2.0 wt% and then slightly decreased to 4.0 wt% due to some extra-framework Mo-oxides.

3.1.2. UV–vis studies

The absorption spectra of Mo-MCM-41 with varying Mo content (0.5–4.0 wt%) are shown in Fig. 2. The absorption bands appeared at around 220–240 nm and 260–300 nm on all of the samples and are assigned to the charge transfer from O^{2-} to Mo^{6+}. The intensity of the absorbance increased with increasing Mo content. The local structures of the Mo-oxides, such as the tetra- and/or hexa-coordinated Mo-oxides, could not be clearly identified by electronic transition because they exhibit a similar energy gap between the HOMO and LUMO levels [46]. However, none of the samples exhibited absorption at wavelengths longer than 340 nm due to the existence of MoO_3, indicating that they have no aggregated MoO_3 species, but rather only highly dispersed Mo-oxides.

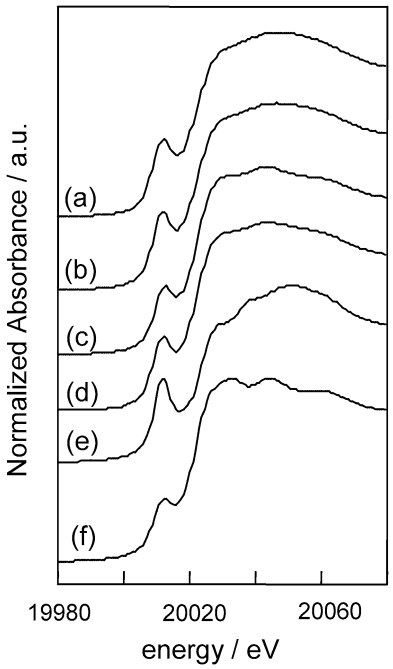

Fig. 3. XANES spectra of Mo-MCM-41 with different Mo contents of (a) 1.0, (b) 2.0, (c) 4.0 wt%, (d) imp-Mo/MCM-41 (1.0 wt%), (e) K_2MoO_4, and (f) MoO_3.

3.1.3. XAFS studies

The normalized Mo *K*-edge XANES spectra of the Mo-MCM-41 (1.0, 2.0, and 4.0 wt%), imp-Mo/MCM-41 (1.0 wt%), K_2MoO_4 with tetra-coordinated molybdate, and MoO_3 with hexa-coordinated molybdate are shown in Fig. 3. In the XANES spectra, a characteristic feature of the pre-edge peak for Mo-MCM-41 was the appearance of a peak due to the so-called "1s–4d transition" of the Mo ions [1]. With low loadings of the Mo content, the shape of the XANES spectra was similar to that of K_2MoO_4. In contrast, with high loadings (4 wt%), the shape of the spectra changed slightly and became similar to that for MoO_3. These results clearly indicate that tetra-coordinated molybdates are formed mainly on Mo-MCM-41 with low loadings of Mo, whereas with high loadings, not only tetra-coordinated molybdates, but also hexa-coordinated molybdates were involved.

The Fourier transforms of the k^3-weighted Mo *K*-edge EXAFS spectra of Mo-MCM-41 (1.0–4.0 wt%) are shown in Fig. 4. Mo-MCM-41 (1.0 wt%) exhibited a peak due to the presence of the neighboring oxygen atoms (Mo–O) at around 0.8–2.0 Å (without phase-shift corrections), and no other characteristic peaks were observed. It was observed that the peaks

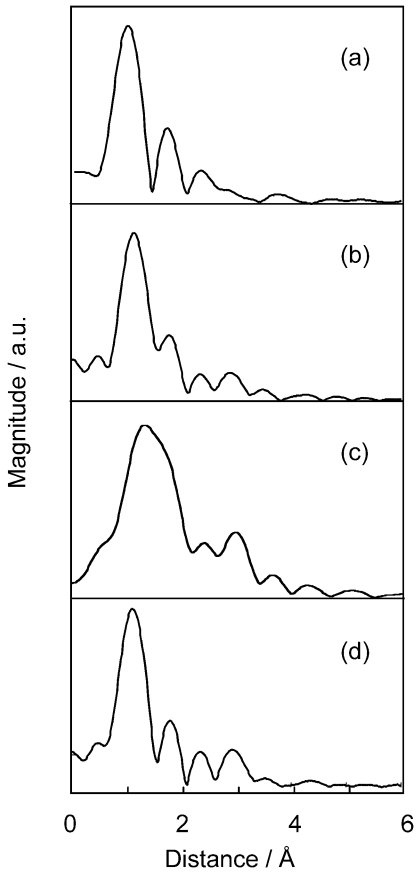

Fig. 4. Fourier-transformed EXAFS spectra of Mo-MCM-41 with different Mo contents of (a) 1.0, (b) 2.0, (c) 4.0 wt%, and (d) imp-Mo/MCM-41 (1.0 wt%).

shifted toward a longer distance, suggesting that the bond length between Mo and O increased with increasing Mo content. Moreover, an intense peak at around 3 Å due to the presence of the neighboring Mo atoms (Mo–O–Mo) was observed in Mo-MCM-41 (4.0 wt%). Curve-fitting analysis of the EXAFS spectra indicated that Mo-MCM-41 (1.0 wt%) involved tetra-coordinated molybdate (MoO_4^{2-}) with two shorter Mo–O bonds (1.68 Å) and two longer Mo–O bonds (1.88 Å), as shown in Table 2. The structures of the molybdate are shown in Scheme 1. The two shorter Mo–O bonds may have a double-bond nature, whereas the two longer bonds have a single-bond nature. These bonding distances increased slightly when the Mo content was increased (1.0–4.0 wt%), indicating that parts of the molybdate in MCM-41 changed from tetrahedral monomer to dimer/oligomer and octahedral polymolybdate. The curve-fitting data show only the averaged values; if different molybdates existed in Mo-MCM-41, then it would be difficult to elucidate the structure of the Mo species from the parameters estimated by the curve-fitting analysis. In the sample with 4 wt% Mo loading, the presence of the neighboring Mo atom through the O bridge bond was detected. Taking the XANES spectrum into consideration, small parts of Mo are seen to exist as hexa-coordinated polymolybdate in Mo-MCM-41 (4 wt%). In addition, the XANES and XAFS spectra show that imp-Mo/MCM-41 (1.0 wt%) involves some hexa-coordinated polymolybdate that differs from Mo-MCM-41 (1.0 wt%).

Table 2
Curve-fitting results of Fourier-transformed EXAFS spectra of Mo-MCM-41 and imp-Mo/MCM41

Samples (wt% as Mo)	Shell	C.N.[a]	R[b] (Å)	σ^{2}[c] (Å^2)
Mo-MCM-41 (1.0)	Mo–O	2.1	1.68	0.005
	Mo–O	1.9	1.88	0.005
Mo-MCM-41 (2.0)	Mo–O	2.1	1.72	0.005
	Mo–O	1.8	1.92	0.005
Mo-MCM-41 (4.0)	Mo–O	2.3	1.74	0.0003
	Mo–O	1.8	1.95	0.0003
	Mo–O–Mo	0.8	3.19	0.0003
imp-Mo/MCM-41 (1.0)	Mo–O	2.1	1.70	0.005
	Mo–O	1.9	1.91	0.005
	Mo–O–Mo	0.4	3.18	0.005

[a] Coordination number.
[b] Inter-atomic distance.
[c] Debye–Waller factor.

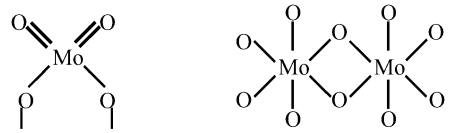

Scheme 1. Model of the (a) monomeric tetra-coordinated molybdate and (b) polymeric hexa-coordinated molybdate.

3.1.4. Photoluminescence studies

$$[Mo^{6+}{=}O^{2-}] \xrightarrow{\text{excitation}} [Mo^{5+}{-}O^{-}]^{*} \xrightarrow{\text{phospho-rescence}} [Mo^{6+}{=}O^{2-}] \quad (1)$$

$$[Mo^{5+}{-}O^{-}]^{*} \xrightarrow{\text{quenching}} [Mo^{5+}{-}O^{-}\cdots Q]$$

(Ground state of tetra-molybdate) (Charge transfer excited triplet state) Q: quencher molecules

Mo-MCM-41 (1.0 wt%) exhibited a phosphorescence spectrum at around 400–600 nm on excitation at around 295 nm recorded at 77 K, coinciding with the phosphorescence spectrum of the tetra-coordinated Mo-oxide species highly dispersed on SiO_2, as shown in Fig. 5. The excitation and emission spectra are attributed to the following electron transfer processes from O^{2-} to Mo^{6+} ions of the tetra-coordinated molybdate (MoO_4^{2-}) and its radiative decay from the charge transfer-excited triplet state to the ground state (Eq. (1)) [8,9].

The shape and wavelength of the phosphorescence spectra at maximum intensity did not change upon varying the excitation wavelengths, indicating that there was only one emitting site defined as the α species. Moreover, the phosphorescence yields were seen to decrease efficiently by the addition of quencher molecules (Q), such as NO, accompanied by a shortened lifetime of the excited state.

In contrast, there were at least two emitting sites on Mo-MCM-41 (4.0 wt%). The absorption spectrum for the phosphorescence can be deconvoluted into two components due to the α and β species having the peak position of the emission excitation spectrum (absorption) at 295 and 310 nm, respectively, as shown in Fig. 6. The imp-Mo/MCM-41 (1.0 wt%) also involved two emitting sites (α and β), although Mo-MCM-41 (1.0 wt%)

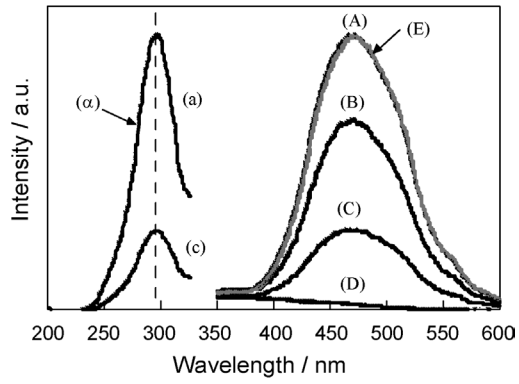

Fig. 5. Effect of the addition of NO on the phosphorescence spectrum and the excitation spectrum of Mo-MCM-41 (1.0 wt% as Mo). Pressure of added NO: (a, A) 0; (B) 0.07; (c, C) 0.4 Torr; (D) excess; (E) degassed after (D).

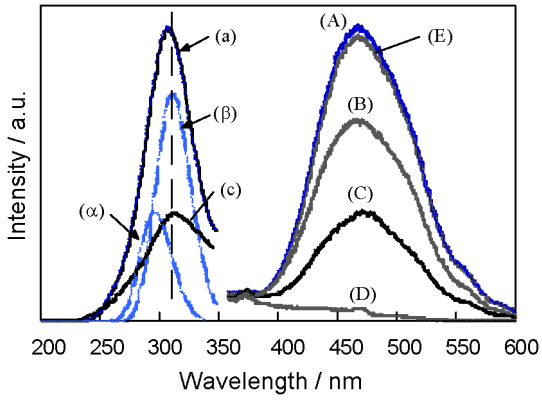

Fig. 6. Effect of the addition of NO on the phosphorescence spectrum and the excitation spectrum of Mo-MCM-41 with 4.0 wt%. Pressure of added NO: (a, A) 0, (B) 0.6, and (c, C) 4 Torr; (D) excess; (E) degassed after (D).

involved only α. The phosphorescence due to α and β was quenched completely by the addition of excess NO, whereas the absorption due to α, in particular, was quenched more efficiently than that of β. The PL studies clearly indicated that two different emitting sites exist, complementing the XAFS study.

The effect of the Mo content on the lifetimes of the charge transfer-excited triplet state, determined from the decay of phosphorescence spectra, was also investigated. In samples with low Mo content (0.5–1.0 wt%), a single exponential decay curve with phosphorescence lifetimes of 2.25–2.26 ms for α was obtained, whereas for the sample with high Mo content (2.0–4.0 wt%), α with lifetimes of 2.27–2.29 ms and β with lifetimes of 0.87–0.91 ms were obtained.

The yield of the phosphorescence increased with a good linearity against the Mo content up to 1.0 wt% with an increase in α concentration, as shown in Fig. 7. At 2.0–4.0 wt%, the concentration of α decreased, whereas the concentration of β increased. It should be noted that imp-Mo/MCM-41 (1.0 wt%) involves α and β, whereas Mo-MCM-41 (1.0 wt%) involves only α even with the same Mo content.

3.2. Photocatalytic reaction of NO with CO

The photocatalytic reduction of NO by CO to form N_2 and CO_2 was also investigated to study the reactivity of these Mo-

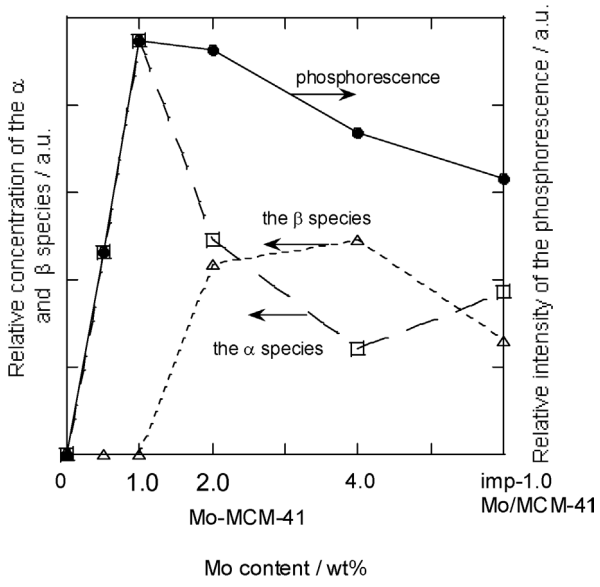

Fig. 7. Effect of the Mo content on the yield of the phosphorescence and the concentration of the α and β species.

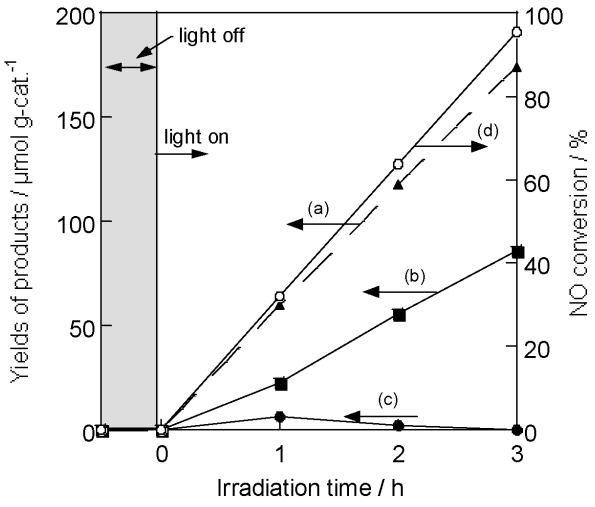

Fig. 8. Reaction time profiles of the photocatalytic reduction of NO in the presence of CO on Mo-MCM-41 (1.0 wt% Mo): yields of (a) CO_2, (b) N_2, (c) N_2O, and (d) conversion of NO.

MCM-41 catalysts. Silicious MCM-41 and MoO_3 itself did not exhibit any reactivity to form N_2 from a NO-CO system under UV light irradiation. The reaction time profiles for the yields of the photo-formed N_2 on Mo-MCM-41 (1.0 wt%) are shown in Fig. 8. The yields of N_2 were found to increase with good linearity against the UV irradiation time, accompanied by the formation of CO_2. The turnover number, defined as the value of the number of photo-formed N_2 molecules divided by the total number of Mo species involved in the used catalyst, exceeded 1.0 after UV irradiation for 2 h on Mo-MCM-41 (1.0 wt%), indicating that the reaction proceeds photocatalytically at 295 K. Moreover, after 3 h of UV irradiation, NO conversion and selectivity for the formation of N_2 reached close to 100% through the formation of small amounts of N_2O during the reaction [42]. The reaction rate constant for N_2 formation were determined at 15.7, 28.7, 26.1, and 24.2 μmol g_{cat}^{-1} h^{-1} on Mo-MCM-41 of 0.5,

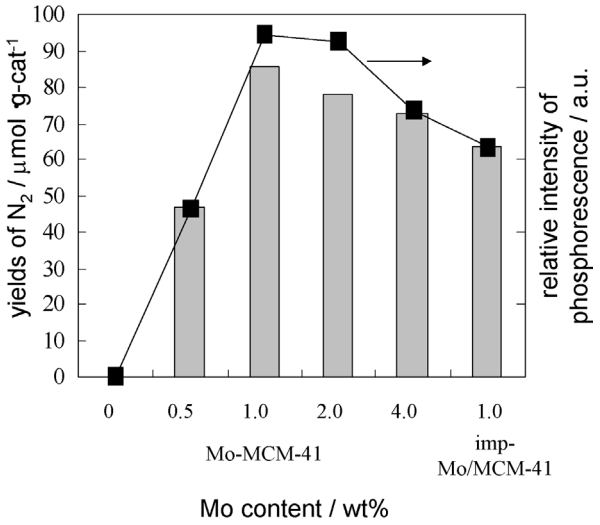

Fig. 9. N_2 yields in the photocatalytic reduction of NO in the presence of CO for 3 h and the phosphorescence yields on Mo-MCM-41 (0, 0.5, 1.0, 2.0, and 4.0 wt%) and imp-Mo/MCM-41 (1.0 wt%).

1.0, 2.0, and 4.0 wt%, respectively, showing a maximum rate in the Mo-MCM-41 with 1.0 wt% Mo content.

The effect of Mo content on the photocatalytic reactivity and the yield of phosphorescence is illustrated in Fig. 9. Photocatalytic reactivity was the highest for Mo-MCM-41 (1.0 wt%), in good correspondence with the phosphorescence yield. The imp-Mo/MCM-41 (1.0 wt%) catalyst showed reactivity similar to that of Mo-MCM-41 (4.0 wt%).

4. Discussion

4.1. Local structures of the Mo-oxides on Mo-MCM-41

In previous work, an anchored Mo/SiO_2 (0.07 wt%) photocatalyst prepared by chemical vapor deposition of vapor $MoCl_5$ with the surface OH group on SiO_2 was observed to involve only one type of emitting site, whereas the impregnated Mo/SiO_2 (0.1 wt%) had at least two different types of emitting sites [25]. Thus the local structure of the Mo-oxides was seen to depend on the sample preparation method. In this work, mesoporous molecular sieves show advantages in the design of photocatalysts with an isolated tetra-coordinated molybdate species with high concentrations, up to 1.0 wt%. Kazansky et al. [22] reported that the lowest excited triplet state of the hexa-coordinated polymeric molybdate causes an efficient radiationless deactivation, leading to the absence of the phosphorescence. Our XAFS and photoluminescence studies indicate that the α species, with an absorption peak at 295 nm, can be assigned to the tetra-coordinated monomeric molybdate on Mo-MCM-41 of up to 1.0 wt%. In fact, the samples with high Mo content (∼2.0 wt%) exhibited a more efficient radiationless energy transfer, leading to a decrease in phosphorescence yields as well as a shortening of the lifetimes attributed to the interactions of Mo–Mo through oxygen bonding (Mo–O–Mo). Based on these results, the β species can be assigned to the tetra-coordinated dimeric and/or oligomeric molybdate, which are favorable due to their clustered structure. XAFS studies showed the coexistence of small parts of hexa-coordinated polymeric molybdate in the sample with higher Mo content (4 wt%), in addition to the α and β species. The local structures of the Ti-oxide were observed to change depending on the Ti content of Ti-MCM-41 [40]. Thus, such changes in the local structure may be applied for various transition metal oxides supported on zeolites and silica.

4.2. Photocatalytic reactivities of the Mo-oxide species

Our results showed that the α species is able to react with quencher molecules such as NO and CO more efficiently than the β species, suggesting that the isolated tetra-coordinated molybdate (α) has better photocatalytic performance than the dimeric and/or oligomeric tetra-coordinated molybdate (β). Comparison of the photocatalytic reactivity for NO–CO per unit of Mo on Mo-MCM-41 showed that the isolated tetra-coordinated molybdate (α) was more reactive than the dimeric and/or oligomeric tetra-coordinated molybdate (β), in good agreement with the results obtained through phosphorescence quenching by NO or CO.

5. Conclusions

Mo-MCM-41 mesoporous molecular sieves with low Mo content (∼1.0 wt%) were found to have only tetra-coordinated monomeric molybdate. However, two different types of tetrahedral Mo species, monomeric and dimeric and oligomeric molybdate, were involved in Mo-MCM-41 with high Mo content (2.0–4.0 wt%). Moreover, hexa-coordinated polymeric molybdates were observed for Mo-MCM-41 when the Mo content was increased to 4.0 wt%. The excited triplet state of the monomeric molybdates was found to interact with the reactant molecules more efficiently than that of the dimer/oligomer species, leading to different photocatalytic reactivities. The photocatalytic performance of Mo-MCM-41 for the reduction of NO with CO to form N_2 and CO_2 was investigated under UV irradiation ($\lambda > 270$ nm) at 295 K. The charge transfer-excited triplet state of the tetra-coordinated molybdate species with monomeric, dimeric and/or oligomeric molybdate species was found to play a significant role in these reactions.

References

[1] Y. Iwasawa (Ed.), X-Ray Absorption Fine Structure for Catalysts and Surfaces, World Scientific, Singapore, 1996, p. 2.
[2] F.E. Massoth, Adv. Catal. 27 (1987) 265.
[3] B. Notari, Adv. Catal. 41 (1996) 253.
[4] Y. Iwasawa, Adv. Catal. 35 (1987) 187.
[5] A. Corma, Chem. Rev. 97 (1997) 2373.
[6] K.I. Zamaraev, J.M. Thomas, Adv. Catal. 41 (1996) 335.
[7] P.B. Simon, R.A.V. Santen, Adv. Catal. 42 (1998) 1.
[8] M. Anpo, M. Che, Adv. Catal. 44 (1999) 119.
[9] M. Anpo (Ed.), Photofunctional Zeolites, NOVA Science Publishers Inc., New York, 2000.
[10] R.W. Borry, Y.H. Kim, A. Huffsmith, J.A. Reimer, E. Iglesia, J. Phys. Chem. B 103 (1999) 5787.
[11] W. Ding, S. Li, G.D. Meitzner, E. Iglesia, J. Phys. Chem. B 105 (2001) 506.

[12] K. Chen, S. Xie, E. Iglesia, A.T. Bell, J. Catal. 189 (2000) 421.
[13] K. Dyrek, M. Che, Chem. Rev. 97 (1997) 305.
[14] C. Louis, M. Che, J. Catal. 135 (1992) 156.
[15] Z. Sojka, M. Che, J. Phys. Chem. 99 (1995) 5418.
[16] M. Che, C. Louis, Z. Sojka, J. Chem. Soc., Faraday Trans. 1 85 (1989) 3939.
[17] P.-S.E. Dai, J.H. Lunsford, J. Catal. 64 (1980) 173.
[18] C. Louis, J.-M. Tatibouët, M. Che, J. Catal. 109 (1988) 354.
[19] C. Louis, M. Che, J. Phys. Chem. 91 (1987) 2875.
[20] C. Li, J. Catal. 216 (2003) 203.
[21] B.N. Shelimov, A.N. Pershin, V.B. Kazansky, J. Catal. 64 (1980) 426.
[22] V.B. Kazansky, Kinet. Katal. 24 (1982) 1338.
[23] B.N. Shelimov, I.V. Elev, V.B. Kazansky, J. Catal. 98 (1986) 70.
[24] S. Takenaka, T. Tanaka, T. Funabiki, S. Yoshida, J. Phys. Chem. B 102 (1998) 2960.
[25] M. Anpo, M. Kondo, S. Coluccia, C. Louis, M. Che, J. Am. Chem. Soc. 111 (1989) 8791.
[26] M. Anpo, I. Tanahashi, Y. Kubokawa, J. Chem. Soc., Faraday Trans. 1 78 (1982) 2121.
[27] M. Anpo, Y. Kubokawa, Res. Chem. Intermed. 8 (1987) 105.
[28] I.R. Subbotina, B.N. Shelimov, M. Che, S. Coluccia, Stud. Surf. Sci. Catal. 140 (2001) 421.
[29] A.A. Lisachenko, K.S. Chikhachev, M.N. Zakharov, L.L. Basov, B.N. Shelimov, I.R. Subbotina, M. Che, S. Coluccia, Top. Catal. 20 (2002) 119.
[30] B. Shelimov, V. Dellarocca, G. Martra, S. Coluccia, M. Che, Catal. Lett. 87 (2003) 73.
[31] M. Anpo, K. Mihara, Y. Kubokawa, J. Catal. 97 (1986) 272.
[32] T. Ono, M. Anpo, Y. Kubokawa, J. Phys. Chem. 90 (1986) 4780.
[33] M. Anpo, M. Kondo, Y. Kubokawa, C. Louis, M. Che, J. Chem. Soc., Faraday Trans. 1 84 (1988) 2771.
[34] M. Matsuoka, M. Anpo, J. Photochem. Photobiol. 3 (2003) 225.
[35] J. Zhang, Y. Hu, M. Matsuoka, H. Yamashita, M. Minagawa, H. Hidaka, M. Anpo, J. Phys. Chem. B 105 (2001) 8395.
[36] H. Yamashita, K. Yoshizawa, M. Ariyuki, S. Higashimoto, M. Che, M. Anpo, J. Chem. Soc., Chem. Commun. (2001) 435.
[37] S. Higashimoto, M. Matsuoka, H. Yamashita, M. Anpo, O. Kitao, H. Hidaka, M. Che, E. Giamello, J. Phys. Chem. B 104 (2000) 10288.
[38] K. Ikeue, H. Yamashita, M. Anpo, J. Phys. Chem. B 105 (2001) 8350.
[39] S. Higashimoto, M. Matsuoka, S.G. Zhang, H. Yamashita, O. Kitao, H. Hidaka, M. Anpo, Micropor. Mesopor. Mater. 48 (2001) 329.
[40] Y. Hu, S. Higashimoto, G. Martra, J. Zhang, M. Matsuoka, S. Coluccia, M. Anpo, Catal. Lett. 90 (2003) 161.
[41] S. Higashimoto, R. Tsumura, S.G. Zhang, M. Matsuoka, H. Yamashita, C. Louis, M. Che, M. Anpo, Chem. Lett. (2000) 408.
[42] R. Tsumura, S. Higashimoto, M. Matsuoka, H. Yamashita, M. Che, M. Anpo, Catal. Lett. 68 (2000) 101.
[43] W. Zhang, J. Wang, P.T. Tanev, T.J. Pinnavaia, J. Chem. Soc., Chem. Commun. (1996) 979.
[44] W. Zhang, M. Froba, J. Wang, P.T. Tanev, J. Wong, T.J. Pinnavaia, J. Am. Chem. Soc. 118 (1996) 9164.
[45] N. Ulagappan, C.N.R. Rao, Chem. Commun. (1996) 1047.
[46] H. Jeziorowski, H. Knözinger, J. Phys. Chem. 83 (1979) 1166.